# ORCHIDEE-MICT (revision 4126), a land surface model for the high-latitudes

Guimberteau et al.

**Soil thermal parameters**

| | $\theta_{\text{sat}}$ (or porosity) $(\text{m}^3\,\text{m}^{-3})$ | $\lambda_{\text{dry}}$ $(\text{W}\,\text{m}^{-1}\,\text{K}^{-1})$ | $\lambda_{\text{solid}}$ $(\text{W}\,\text{m}^{-1}\,\text{K}^{-1})$ | $c_{\text{dry}}$ $(10^6\,\text{J}\,\text{K}^{-1}\,\text{m}^{-3})$ |
|---|---|---|---|---|
| sand | 0.43 | 0.22 | 6.91 | 1.47 |
| loamy sand | 0.41 | 0.23 | 6.04 | 1.41 |
| sandy loam | 0.41 | 0.23 | 4.49 | 1.34 |
| silt loam | 0.45 | 0.20 | 2.80 | 1.27 |
| silt | 0.46 | 0.20 | 3.30 | 1.21 |
| loam | 0.43 | 0.22 | 3.43 | 1.21 |
| sandy clay loam | 0.39 | 0.25 | 4.49 | 1.18 |
| silty clay loam | 0.43 | 0.22 | 3.30 | 1.32 |
| clay loam | 0.41 | 0.23 | 3.21 | 1.23 |
| sandy clay | 0.38 | 0.26 | 4.03 | 1.18 |
| silty clay | 0.36 | 0.28 | 3.30 | 1.15 |
| clay | 0.38 | 0.26 | 2.80 | 1.09 |
| pure organic soil | 0.92 | 0.05 | 0.25 | 2.50 |

$\theta_{\text{sat}}$: volumetric moisture content at saturation (porosity); $\lambda_{\text{dry}}$ : dry soil thermal conductivity, calculated by the empirical equation:

$\lambda_{\text{dry}} = \frac{0.135\rho + 64.7}{2700 - 0.947\rho}$ with $\rho = 2700\,(1 - \theta_{\text{sat}})$

$\lambda_{\text{solid}}$ : thermal conductivity of soil solids; $c_{\text{dry}}$ : dry soil heat capacity.

**Table S1.** Soil thermal parameters for mineral soil (including 12 USDA soil textures) and organic soil used in Eq. 4.

**Soil hydraulic parameters**

| | $\theta_r$ (m$^3$ m$^{-3}$) | $\alpha$ | n | $\theta_{fc}$ (m$^3$ m$^{-3}$) | $\theta_{wp}$ (m$^3$ m$^{-3}$) |
|---|---|---|---|---|---|
| sand[a] | 0.045 | 1.45 | 2.68 | 0.049 | 0.045 |
| loamy sand[a] | 0.057 | 1.24 | 2.28 | 0.071 | 0.057 |
| sandy loam[a] | 0.065 | 0.75 | 1.89 | 0.122 | 0.066 |
| silt loam | 0.067 | 0.20 | 1.41 | 0.240 | 0.104 |
| silt | 0.034 | 0.16 | 1.37 | 0.258 | 0.090 |
| loam | 0.078 | 0.36 | 1.56 | 0.165 | 0.088 |
| sandy clay loam | 0.100 | 0.59 | 1.48 | 0.169 | 0.111 |
| silty clay loam | 0.089 | 0.10 | 1.23 | 0.338 | 0.197 |
| clay loam | 0.095 | 0.19 | 1.31 | 0.270 | 0.150 |
| sandy clay | 0.100 | 0.27 | 1.23 | 0.267 | 0.170 |
| silty clay | 0.070 | 0.05 | 1.09 | 0.337 | 0.266 |
| clay | 0.068 | 0.08 | 1.09 | 0.347 | 0.271 |

**Table S2.** Coefficients in the van Genuchten equation (Eq. 11) and derived field capacity ($\theta_{fc}$) and permanent wilting point ($\theta_{wp}$) for the 12 USDA soil textures. [a]: for the three sandy soils, field capacity corresponds to $\psi = -10\,\text{kPa}$ instead of -33 kPa.

**Number of ignitions in the SPITFIRE module in ORCHIDEE-MICT**

| Region | BONA | TENA | CEAM | NHSA | SHSA | EURO | MIDE | NHAF | SHAF | BOAS | CEAS | SEAS | EQAS | AUST |
|---|---|---|---|---|---|---|---|---|---|---|---|---|---|---|
| Ratio | 2.09 | 0.04 | 1.02 | 0.62 | 0.67 | 1.20 | 2.85 | 56.24 | 31.67 | 3.39 | 1.68 | 12.64 | 99.80 | 3.56 |

**Table S3.** Region-specific values used to scale the simulated number of ignitions in the SPITFIRE module in ORCHIDEE-MICT. Refer to http://www.globalfiredata.org/data.html for the acronyms of different regions.

**Selected northern watersheds for discharge and water balance evaluation**

| Station name | Basin name | Longitude (°E) | Latitude (°N) | Basin area (km²) | $Q_{mean}$ GRDC ($m^3 s^{-1}$) | Naturalized $Q_{mean}$ ($m^3 s^{-1}$) | Permafrost area (%) |
|---|---|---|---|---|---|---|---|
| Pilot station | Yukon | -162.88 | 61.93 | 831390 | 6553 | - | 87 |
| Arctic Red River | Mackenzie | -133.75 | 67.46 | 1660000 | 9044 | - | 42 |
| Volgograd Power Plant | Volga | 44.59 | 48.81 | 1360000 | 8246 | - | - |
| Salekhard | Ob | 66.53 | 66.57 | 2949998 | 12960 | 13005 | 4 |
| Igarka | Yenisei | 86.50 | 67.48 | 2440000 | 19400 | 19234 | 42 |
| Kusur | Lena | 127.65 | 70.70 | 2430000 | 17550 | 17426 | 90 |
| Kolymskaya | Kolyma | 158.72 | 68.73 | 526000 | 3252 | - | 100 |

**Table S4.** List of the gauge stations of the seven major Arctic rivers studied. $Q_{mean}$ is the mean annual discharge from the two databases, averaged over the period 1981-2007. Permafrost coverage (continuous + discontinuous permafrost) is calculated using data from Brown et al. (1998) over the entire basin considered (Holmes et al., 2012).

**Relationships between river discharge bias in Spring and pre-melt SWE bias**

| Basin name | Pre-melt SWE bias ($m^3 s^{-1}$) [average Feb.-Mar.] | | Spring flow bias ($m^3 s^{-1}$) [sum Apr.-Jun.] | | Spring flow bias explained by the pre-melt SWE bias (%) | |
|---|---|---|---|---|---|---|
| | GSWP3 | CRUNCEP | GSWP3 | CRUNCEP | GSWP3 | CRUNCEP |
| 1: Yukon | +1825 | -6420 | +13180 | -18900 | 14 | 34 |
| 2: Mackenzie | +2700 | -3200 | +38350 | +1880 | 7 | -170 |
| 3: Volga | +9140 | +2615 | +57360 | +30030 | 16 | 9 |
| 4: Ob | +11825 | -3510 | +64960 | +30730 | 18 | -11 |
| 5: Yenisei | +6235 | -4730 | +6430 | -46470 | 97 | 10 |
| 6: Lena | -530 | -9515 | +18160 | -39550 | -3 | 24 |
| 7: Kolyma | +560 | -2580 | +4430 | -11175 | 13 | 23 |

**Table S5.** SWE bias during the pre-melt season (average between February and March) and the bias of discharge in spring (total discharge between April and June) (both in $m^3 s^{-1}$) with the two forcings in each basin, over the period 1981-2007. The two last columns are the contribution of the pre-melt SWE bias to the spring discharge bias (in %). Bias is defined here exactly like in Fig. 23.

**Soil vertical discretization in ORCHIDEE-MICT**
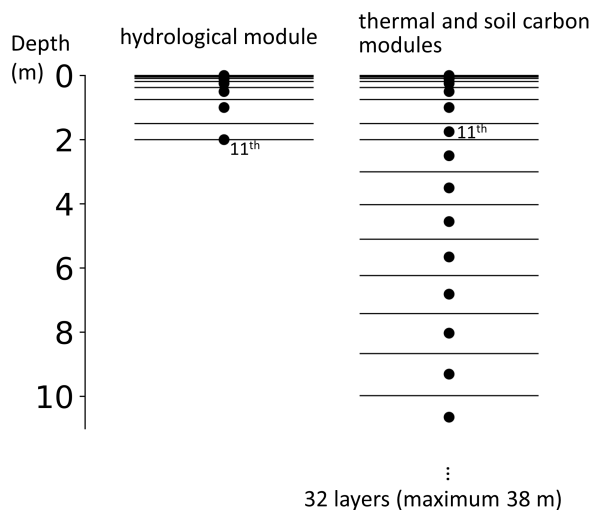
**Figure S1.** Soil vertical discretization in ORCHIDEE-MICT. Solid lines and black dots represent the interfaces and nodes of each layer respectively. The soil hydrological module has 11 layers to 2 meters; the soil thermal and soil carbon modules have 32 layers to 38 meters, in which the first 11 layers are identical to that in hydrology, except that the nodes of the 1st and 11th layer in hydrology lie at the interface.

**Soil moisture content as a function of soil organic carbon**
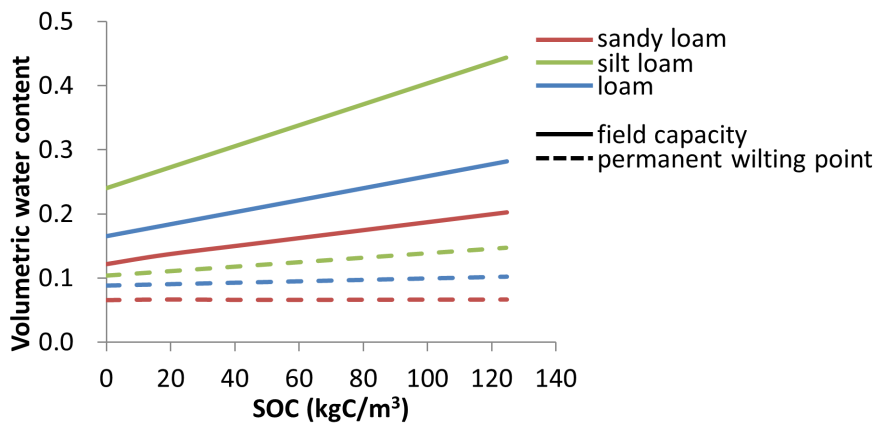
**Figure S2.** Parameterization of soil moisture content at field capacity ($\theta_{fc}$) and permanent wilting point ($\theta_{wp}$) as a function of soil organic carbon, for three representative soil textures in the northern high latitudes. The difference between $\theta_{fc}$ and $\theta_{wp}$ represents the water holding capacity of the soil as a function of SOC.
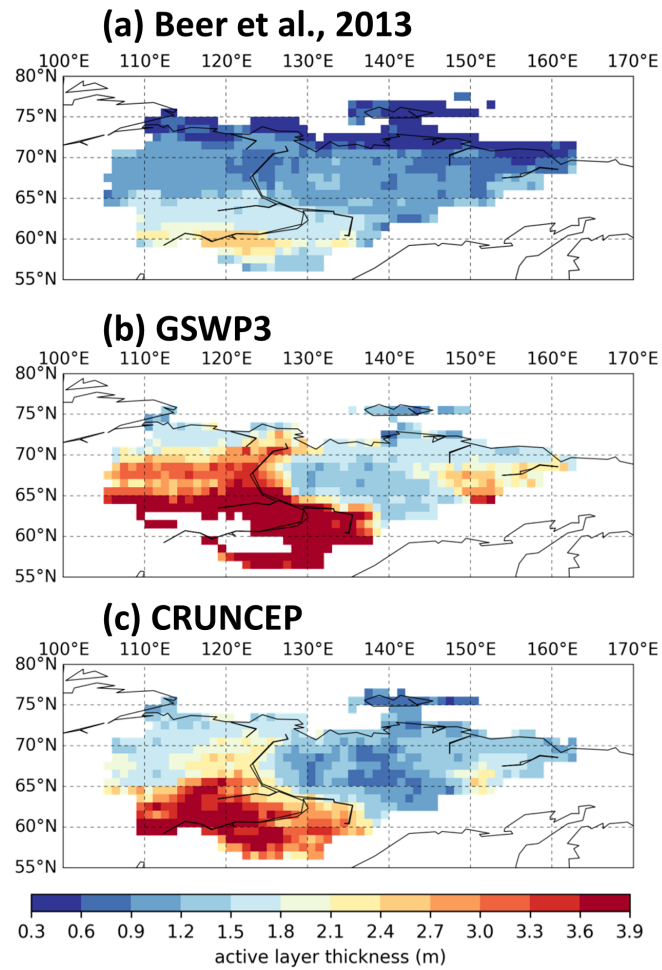
**Figure S3. (a)** Active layer thickness (ALT) of Yakutia, East Siberia, upscaled based on the map of landscapes and permafrost conditions in Yakutia by Beer et al. (2013). **(b,c)** Modeled ALT for the same region with GSWP3 and CRUNCEP, averaged over the period 1960-1987 to be consistent with Beer et al. (2013).

**Albedo**
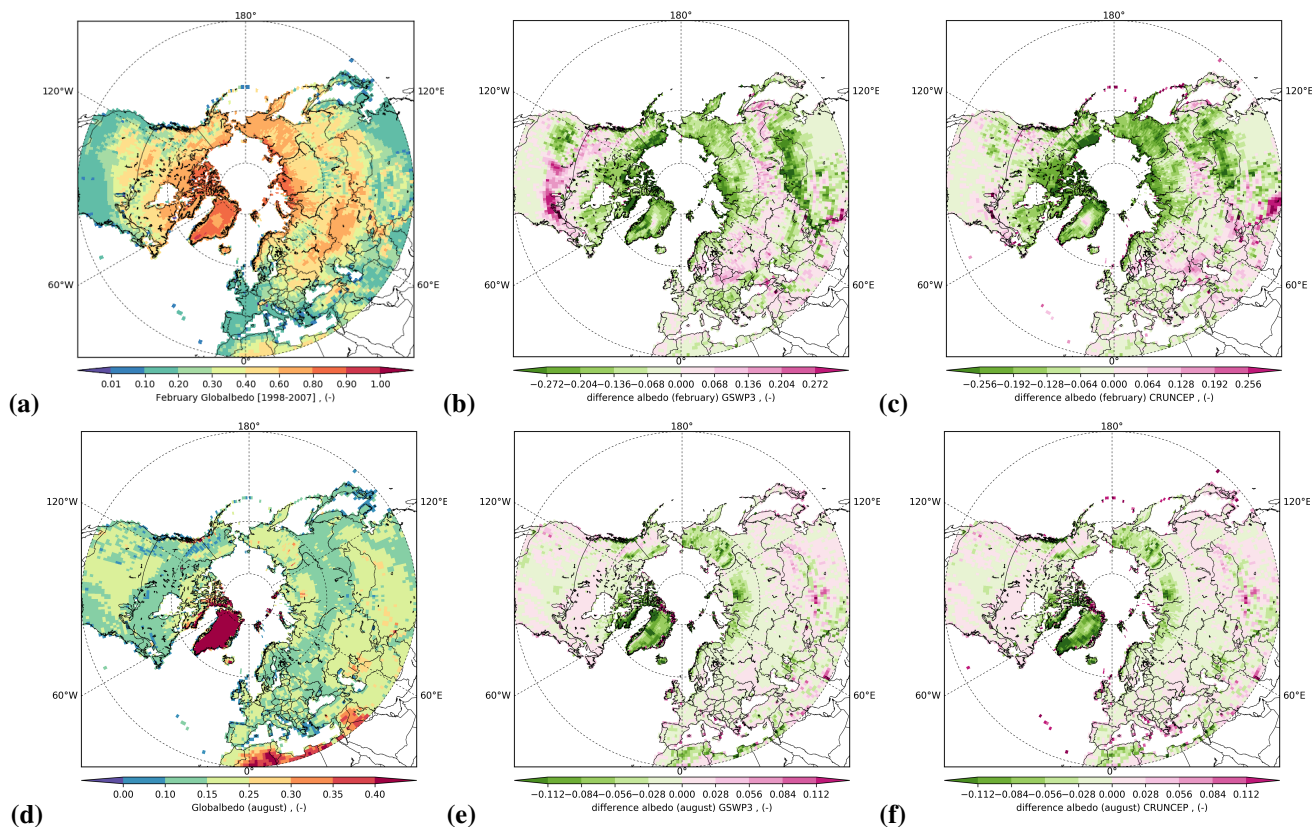
**Figure S4.** Albedo **(left)** observed (ESA-GlobAlbedo) for the months of **(Upper panel)** February and **(Lower panel)** August, averaged over the period 1998-2011. Albedo bias with **(middle)** GSWP3 and **(right)** CRUNCEP climate forcing.

In February, when the snow cover is maximum, the plots show an overall underestimation of the modeled albedo up to 0.25 in the snow-covered regions particularly with CRUNCEP forcing and a slight overestimation elsewhere (Fig. S4). These differences may be partly explained by the SWE underestimation already highlighted and also by weaknesses in the parametrization of the albedo, especially over high vegetation (forested areas in North America, central Europe and Siberia). In these forested regions, the albedo seems to be overestimated in presence of snow. In August, the comparison shows very similar values in the modeled product whatever the atmospheric forcing used and the differences with the observations are strongly related to the land cover map. Grasslands in the northern regions presents underestimated albedo values up to 0.1, whereas the albedo is overestimated slightly elsewhere with a bias of about +0.02. These discrepancies may be explained by the LAI summer lag already discussed which leads to an overestimation of the vegetation cover in August and consequently an underestimation of the albedo (since the albedo of bare soils is generally larger than those of vegetation).

**Latitudinal distribution of fire carbon emissions**
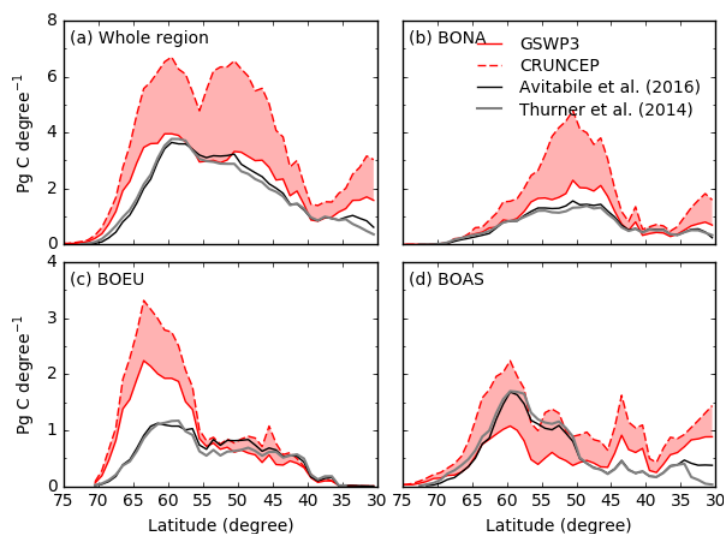
**Figure S5.** Latitudinal distribution of total annual forest biomass carbon stocks (PgC degree$^{-1}$) in the GSWP3 and CRUNCEP-forced simulations, compared to observations by Avitabile et al. (2016) and Thurner et al. (2014) for **(a)** the whole model domain. High-latitude sub-regions of **(b)** BONA, **(c)** BOEU and **(d)** BOAS have been extended to 30°N here compared to their shapes in Fig. 2a.

**Seasonal cycle of burned area and fire carbon emissions**
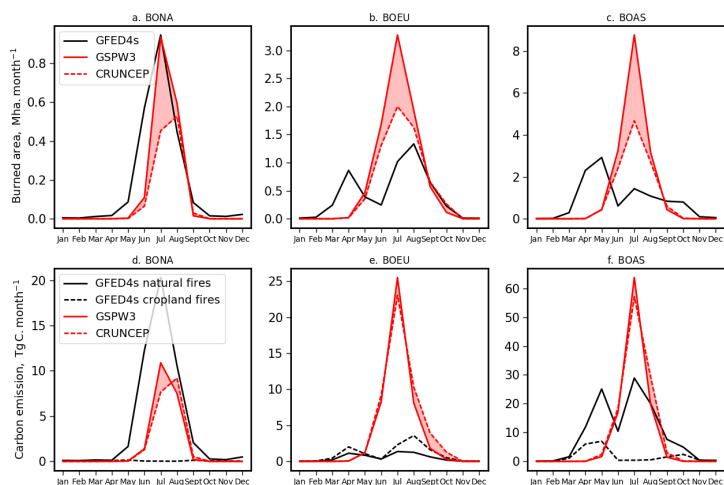
**Figure S6.** Monthly mean seasonal **(a-c)** fire burned area (Mha month$^{-1}$) and **(d-f)** carbon emissions to the atmosphere (TgC month$^{-1}$) from the GFED4s dataset and the two simulations, averaged over the period 1997–2007. For carbon emissions, cropland and natural fires are represented separately.

# LAI and GPP seasonality between deciduous and evergreen forests
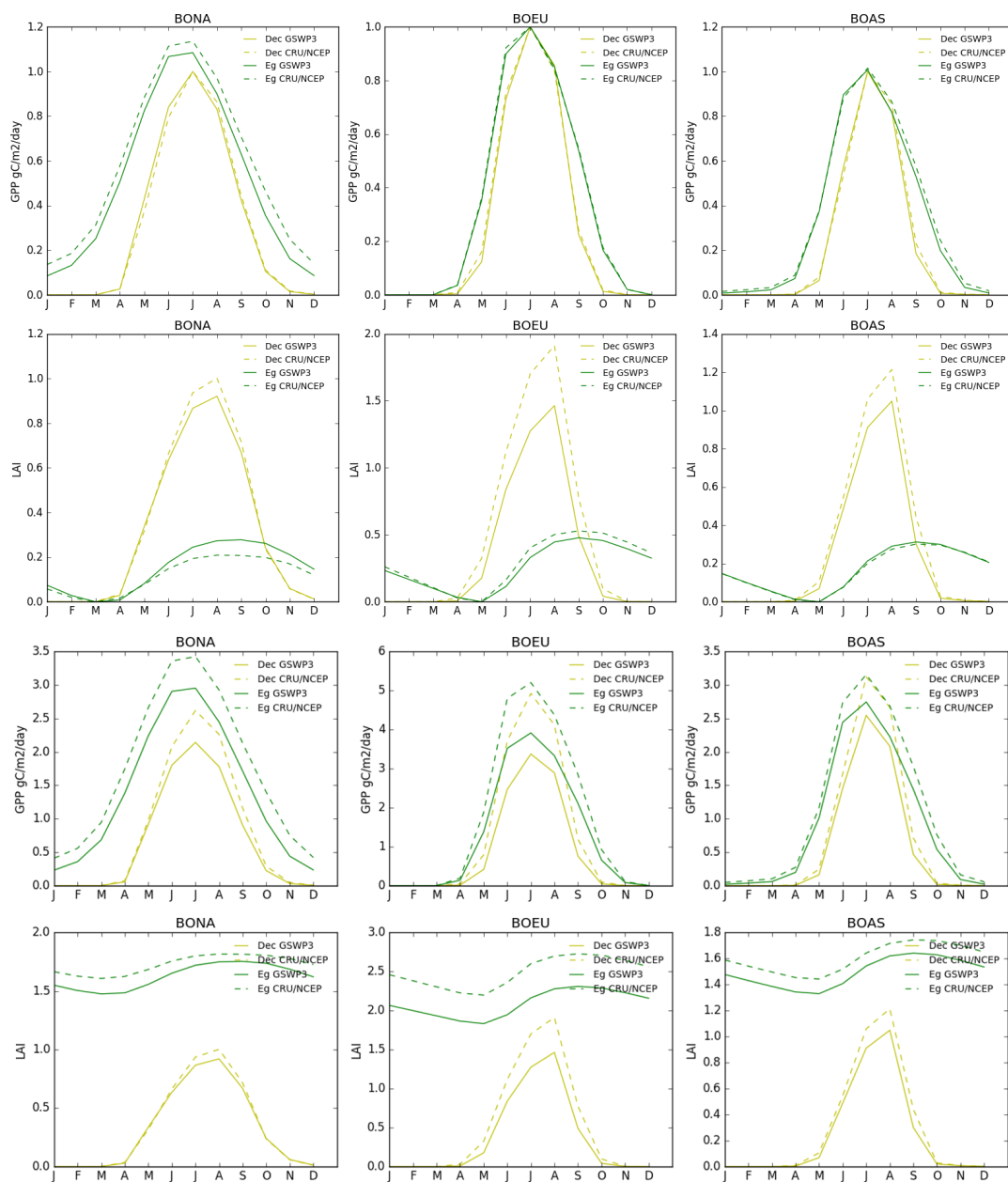
**Figure S7.** Monthly mean seasonal **(first and third panels)** GPP ($gC\,m^{-2}\,day^{-1}$) and **(second and fourth panels)** LAI (-) for deciduous (light green) and conifer forests (dark green), over the three high-latitude sub-regions (shown in Fig. 2a), averaged over the period 2000-2007. The lower panel shows absolute values and the upper one values scaled for a better comparison.

**Land carbon fluxes and pools modeled and derived from observations**
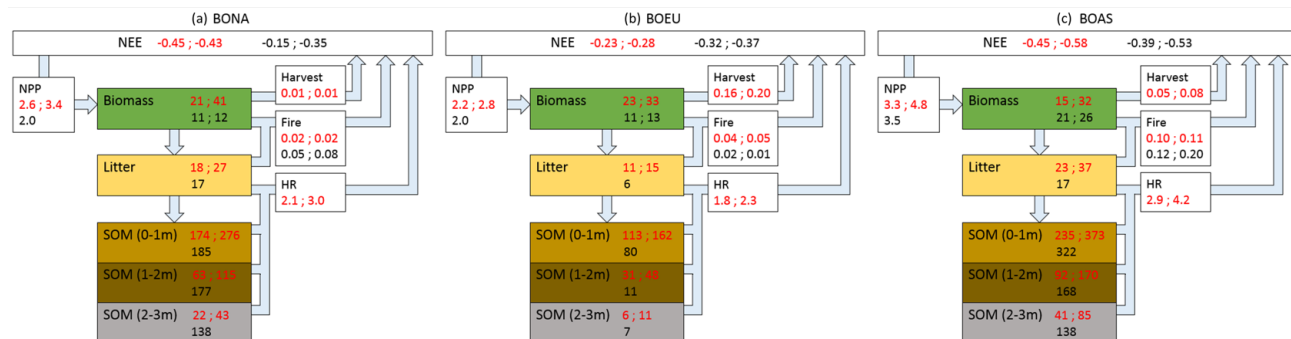
**Figure S8.** Annual mean land carbon fluxes (PgC yr$^{-1}$) and pool sizes (PgC) over the three high-latitude sub-regions (shown in Fig. 2a) **(a)** BONA, **(b)** BOEU and **(c)** BOAS, averaged over the period 2000-2007. The red numbers are the model results forced by (left) GSWP3 and (right) CRUNCEP. The black numbers are from observation-based estimates used in the text : NPP from MODIS (NTSG), fire emissions from (left) GFED4s and (right) GFAS datasets, harvest fluxes include crop harvest and wood product decay in the model (for simplicity the change in wood product pools is not represented), NEE from the two atmospheric inversions (left) Jena CarboScope and (right) CAMS, biomass from (left) Avitabile et al. (2016) and (right) Thurner et al. (2014), litter from Pan et al. (2011), soil carbon from NCSCD (Hugelius et al., 2013) in permafrost regions and HWSD in non-permafrost regions.

**Differences of atmospheric variables between GSWP3 and CRUNCEP forcings**
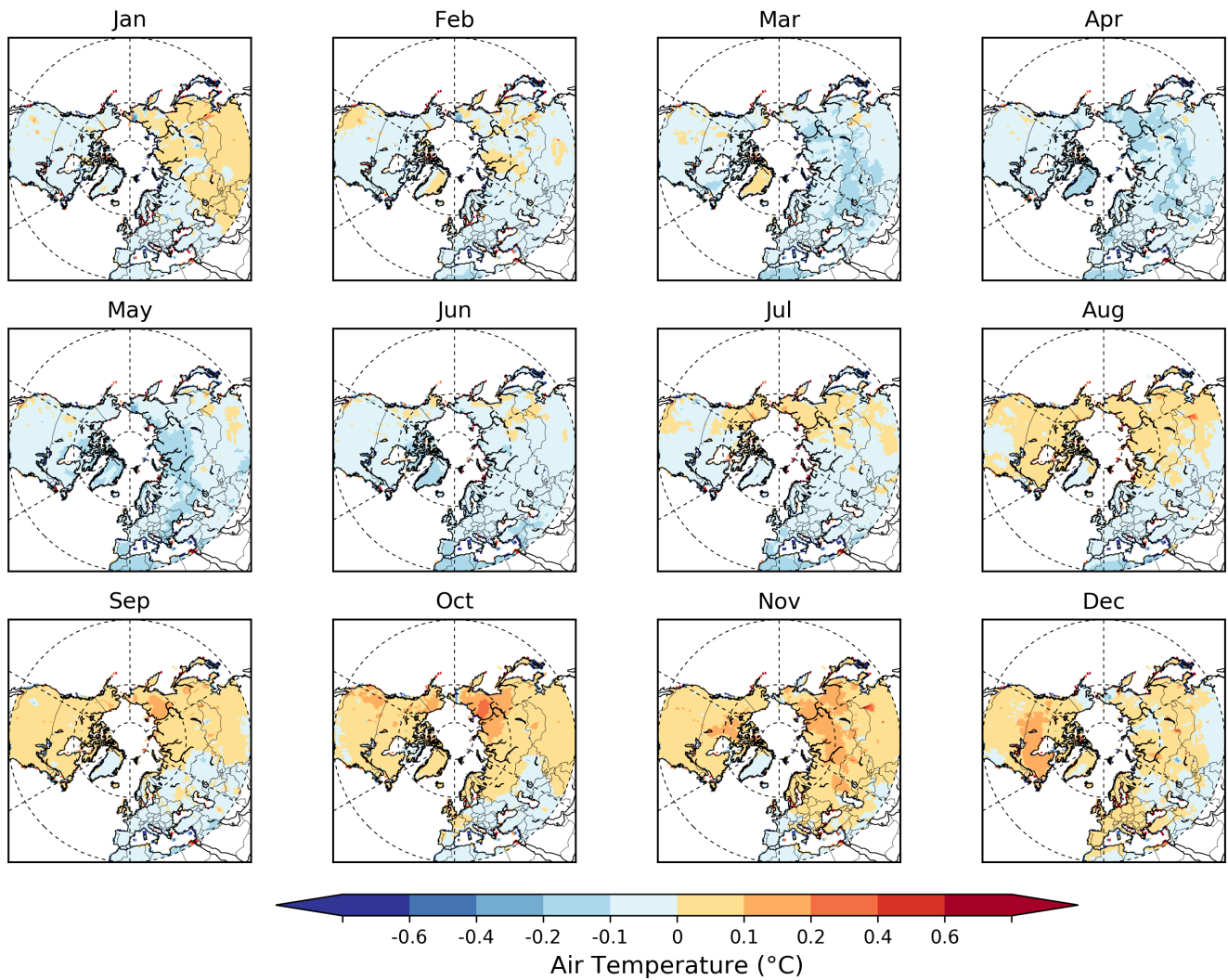
**Figure S9.** Difference in monthly air temperature (°C) between GSWP3 and CRUNCEP, averaged over the period 1981-2007.
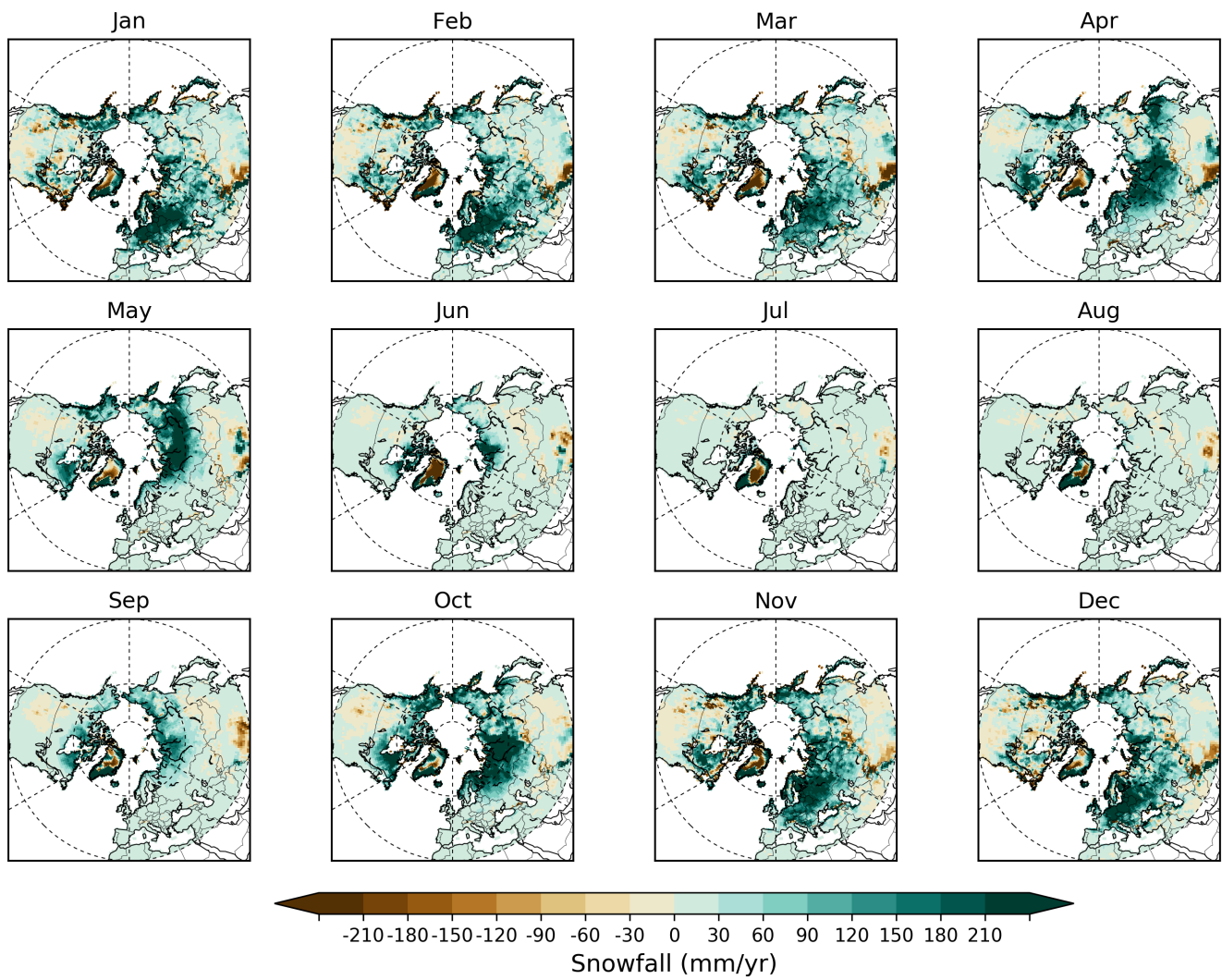
**Figure S10.** Same as Fig. S9 but for snowfall ($mm\,yr^{-1}$)
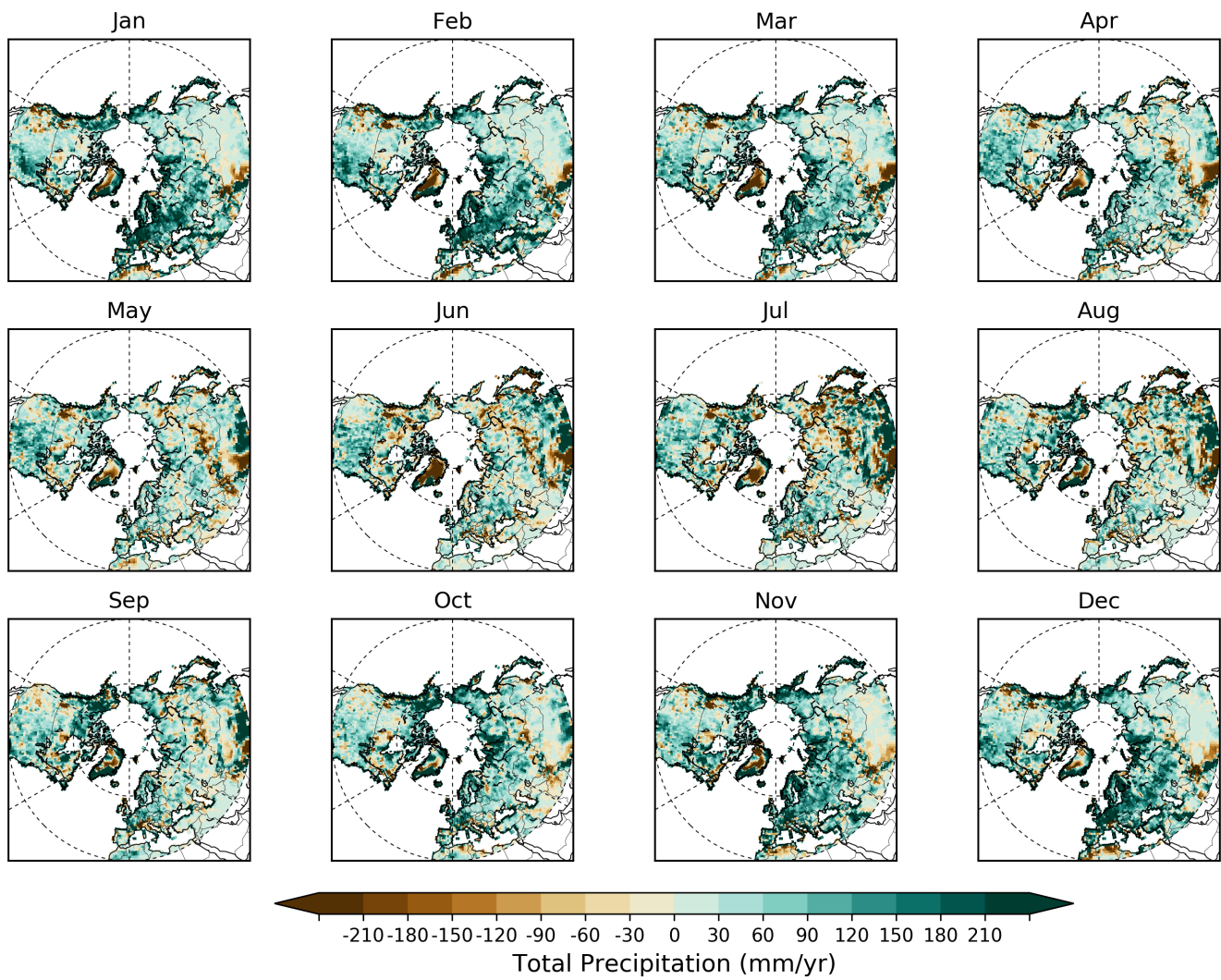
**Figure S11.** Same as Fig. S9 but for total precipitation (mm yr$^{-1}$)
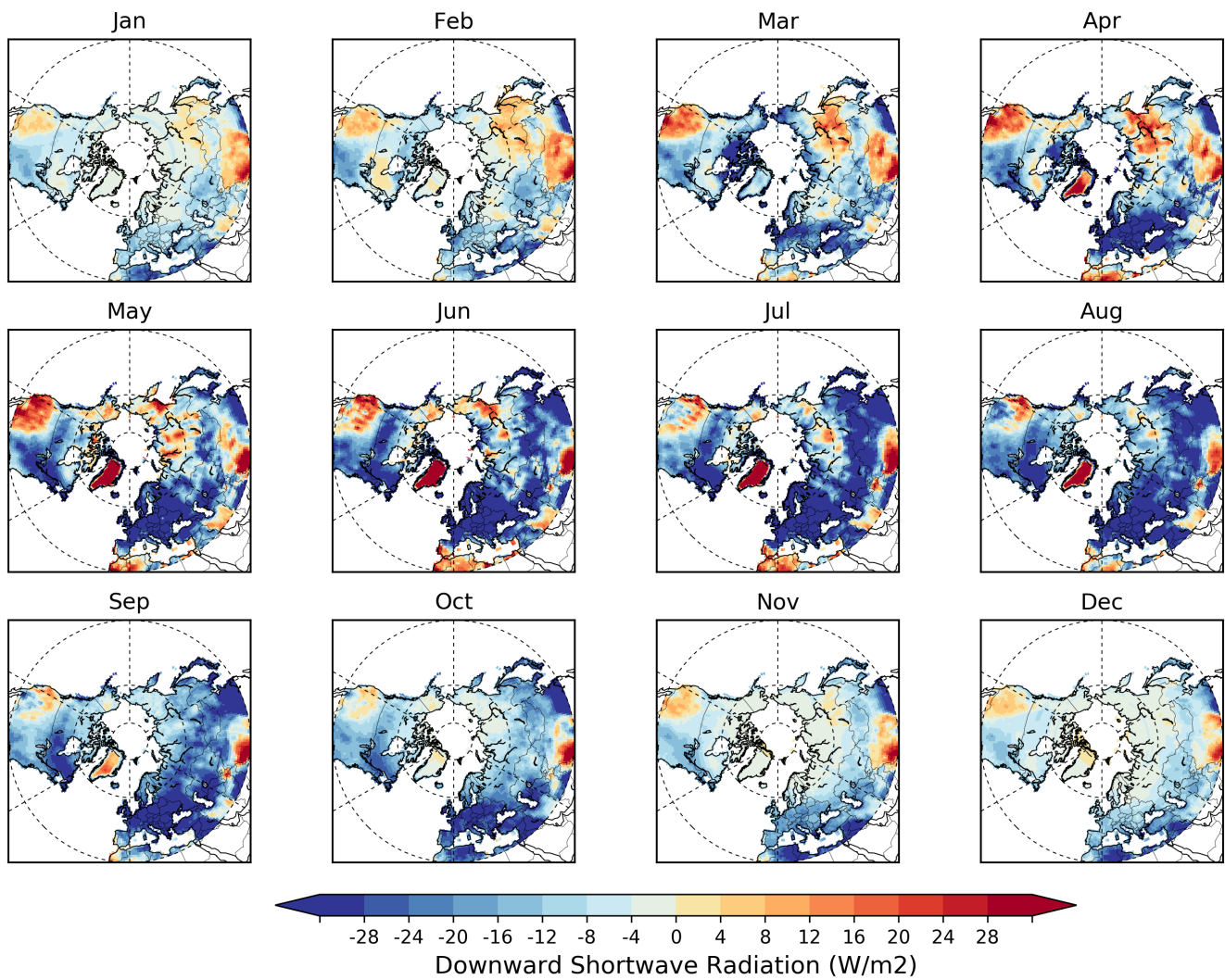
**Figure S12.** Same as Fig. S9 but for downward shortwave radiation (W m$^{-2}$)
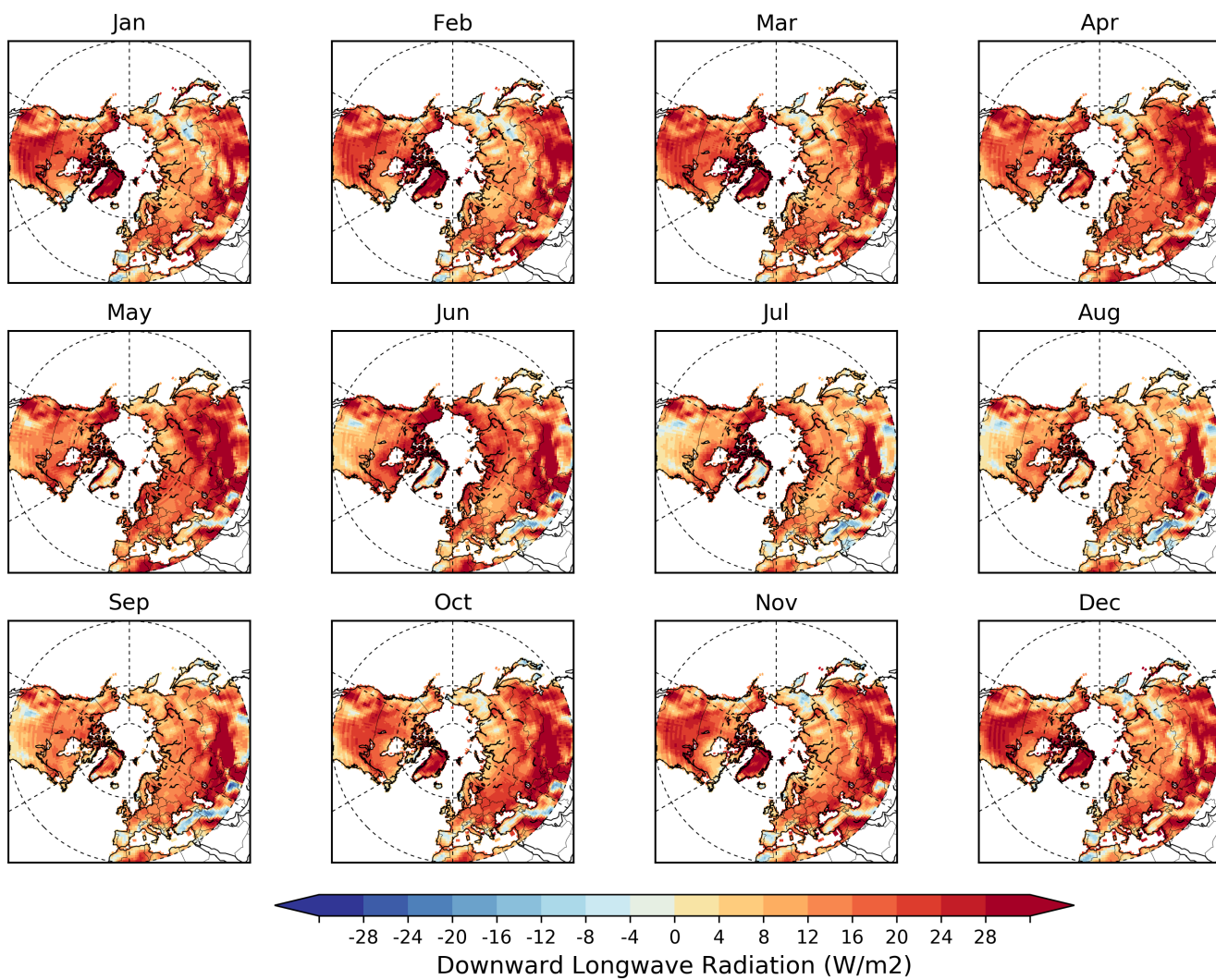
**Figure S13.** Same as Fig. S9 but for downward longwave radiation ($\mathrm{W\,m^{-2}}$)
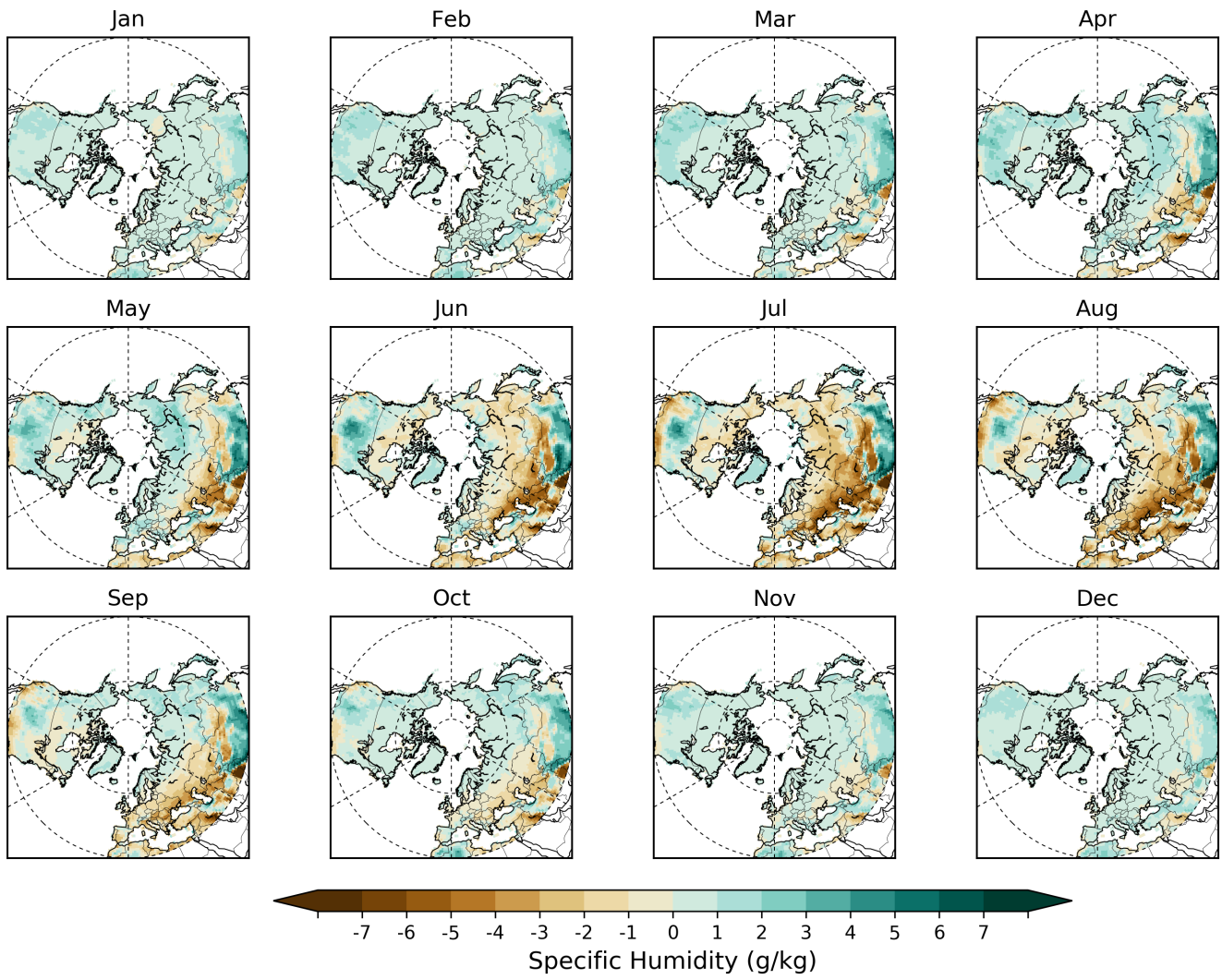
**Figure S14.** Same as Fig. S9 but for specific humidity ($\mathrm{g\,kg^{-1}}$)
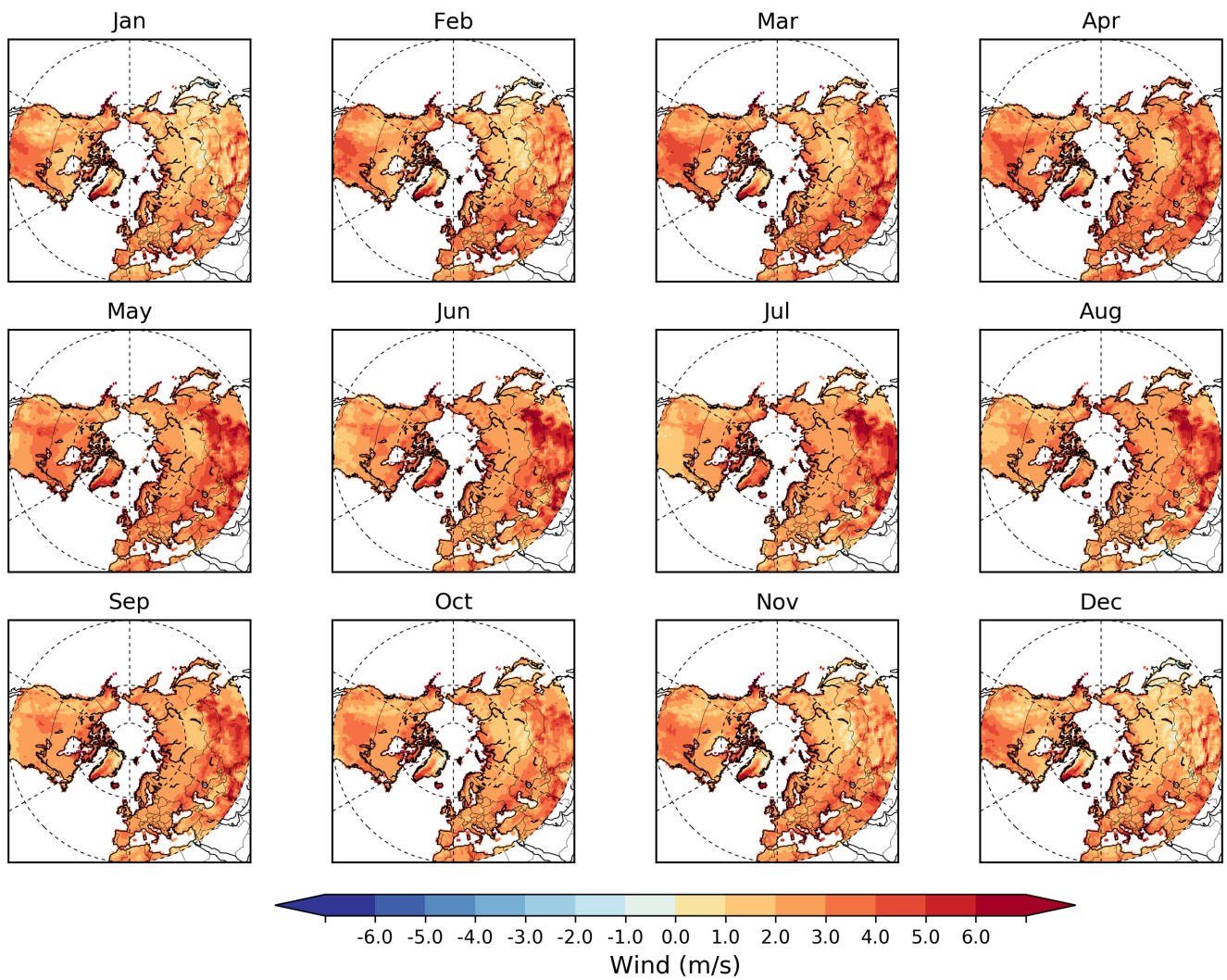
**Figure S15.** Same as Fig. S9 but for wind speed at 10 m ($\mathrm{m\,s^{-1}}$)
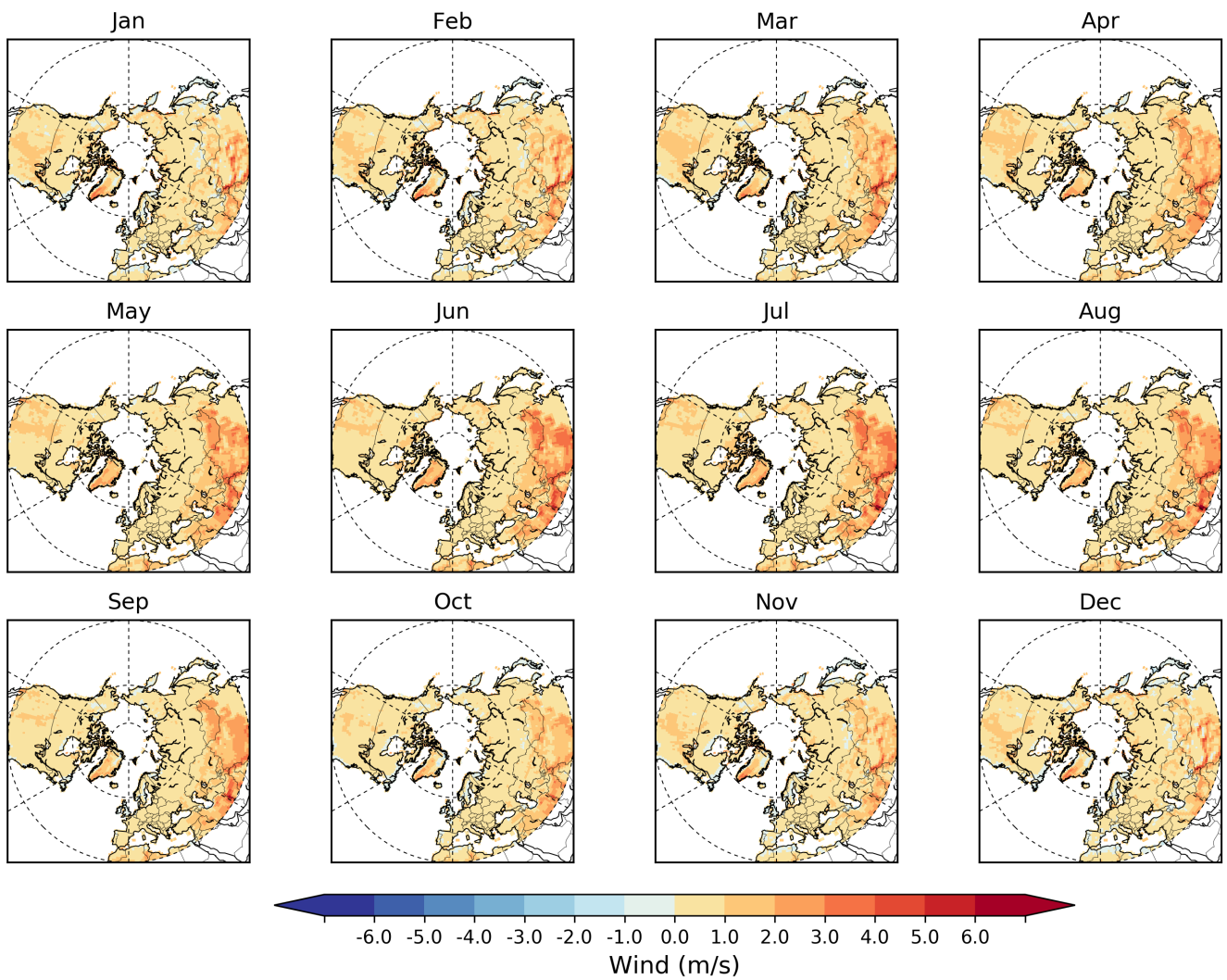
**Figure S16.** Same as Fig. S9 but for wind speed at 2 m in ORCHIDEE outputs ($m\,s^{-1}$)

# References

Avitabile, V., Herold, M., Heuvelink, G. B. M., Lewis, S. L., Phillips, O. L., Asner, G. P., Armston, J., Ashton, P. S., Banin, L., Bayol, N., Berry, N. J., Boeckx, P., de Jong, B. H. J., DeVries, B., Girardin, C. A. J., Kearsley, E., Lindsell, J. A., Lopez-Gonzalez, G., Lucas, R., Malhi, Y., Morel, A., Mitchard, E. T. A., Nagy, L., Qie, L., Quinones, M. J., Ryan, C. M., Ferry, S. J. W., Sunderland, T., Laurin, G. V., Gatti, R. C., Valentini, R., Verbeeck, H., Wijaya, A., and Willcock, S.: An integrated pan-tropical biomass map using multiple reference datasets, Glob. Change Biol., 22, 1406–1420, doi:10.1111/gcb.13139, 2016.

Beer, C., Fedorov, A. N., and Torgovkin, Y.: Permafrost temperature and active-layer thickness of Yakutia with 0.5-degree spatial resolution for model evaluation, Earth Syst. Sci. Data, 5, 305–310, doi:10.5194/essd-5-305-2013, http://www.earth-syst-sci-data.net/5/305/2013/, 2013.

Brown, J., Ferrians Jr, O., Heginbottom, J., and Melnikov, E.: Revised February 2001. Circum-Arctic map of permafrost and ground-ice conditions. Boulder, CO: National Snow and Ice Data Center/World Data Center for Glaciology, Digital media, 1998.

Holmes, R. M., McClelland, J. W., Peterson, B. J., Tank, S. E., Bulygina, E., Eglinton, T. I., Gordeev, V. V., Gurtovaya, T. Y., Raymond, P. A., Repeta, D. J., Staples, R., Striegl, R. G., Zhulidov, A. V., and Zimov, S. A.: Seasonal and Annual Fluxes of Nutrients and Organic Matter from Large Rivers to the Arctic Ocean and Surrounding Seas, Estuaries Coasts, 35, 369–382, doi:10.1007/s12237-011-9386-6, 2012.

Hugelius, G., Tarnocai, C., Broll, G., Canadell, J., Kuhry, P., and Swanson, D.: The Northern Circumpolar Soil Carbon Database: spatially distributed datasets of soil coverage and soil carbon storage in the northern permafrost regions, Earth Syst. Sci. Data, 5, 3, doi:10.5194/essdd-5-707-2012, 2013.

Pan, Y., Chen, J. M., Birdsey, R., McCullough, K., He, L., and Deng, F.: Age structure and disturbance legacy of North American forests, Biogeosciences, 8, 715, doi:10.5194/bg-8-715-2011, 2011.

Thurner, M., Beer, C., Santoro, M., Carvalhais, N., Wutzler, T., Schepaschenko, D., Shvidenko, A., Kompter, E., Ahrens, B., Levick, S. R., and Schmullius, C.: Carbon stock and density of northern boreal and temperate forests, Global Ecol. Biogeogr., 23, 297–310, doi:10.1111/geb.12125, http://dx.doi.org/10.1111/geb.12125, 2014.